AGU PUBLICATIONS

Geophysical Research Letters

RESEARCH LETTER
10.1002/2014GL061016

Key Points:
- A new database for the characterization of frozen precipitation is presented
- Riming is associated with more compact particles that fall faster
- Fallspeed is determined by temperature, turbulence, and particle size and shape

Correspondence to:
T. J. Garrett,
tim.garrett@utah.edu

Citation:
Garrett, T. J., and S. E. Yuter (2014), Observed influence of riming, temperature, and turbulence on the fallspeed of solid precipitation, *Geophys. Res. Lett.*, *41*, doi:10.1002/2014GL061016.

Received 4 JUL 2014
Accepted 25 AUG 2014
Accepted article online 27 AUG 2014

Observed influence of riming, temperature, and turbulence on the fallspeed of solid precipitation

Timothy J. Garrett[1] and Sandra E. Yuter[2]

[1]Department of Atmospheric Sciences, University of Utah, Salt Lake City, Utah, USA, [2]Marine, Earth, and Atmospheric Sciences, North Carolina State University, Raleigh, North Carolina, USA

Abstract Forecasts of the amount and geographic distribution of snow are highly sensitive to a model's parameterization of hydrometeor fallspeed. Riming is generally thought to lead to particles with a higher mass and terminal velocity. Yet models commonly assume that heavily rimed particles such as graupel have a fixed density and that their settling speed is unaffected by turbulence in storms. Here we show automated measurements of photographed hydrometeor shape and fallspeed using a new instrument placed in Utah's Wasatch Mountain Range. The data show that graupel in low-turbulence conditions has a size-dependent fallspeed distribution with a mode near 1 m s^{-1}, a result that is generally consistent with prior observations. However, the distributions are broadened by turbulence and there is a correspondence between particle density and air temperature. In high turbulence and at low temperatures, any sensitivity of fallspeed to particle size disappears.

1. Introduction

Solid precipitation is a critical component of any weather or climate model since predictions of precipitation amount, location, and duration depend greatly on how precipitation particles are parameterized to grow and fall [*Rutledge and Hobbs*, 1984; *Lin et al.*, 1983; *Reisner et al.*, 1998; *Hong et al.*, 2004; *Garvert et al.*, 2005; *Colle et al.*, 2005; *Lin et al.*, 2010; *Milbrandt et al.*, 2010; *Lin and Colle*, 2011; *Liu et al.*, 2011; *Iguchi et al.*, 2012; *Thériault et al.*, 2012b]. Unfortunately, few direct measurements of the fallspeed of solid precipitation have been made. Parameterizations that relate condensate amount to fallspeed [e.g., *Reisner et al.*, 1998; *Hong et al.*, 2004; *Tao et al.*, 2003] can often be traced to a single-decade old empirical study from the Cascade Mountain Range by *Locatelli and Hobbs* [1974] (LH74) that were based on just a few tens of data points per ice particle habit.

Greater generality has been sought by considering hydrometeor fluid dynamics [*Böhm*, 1989; *Mitchell*, 1996; *Khvorostyanov and Curry*, 2002; *Heymsfield and Westbrook*, 2010; *Kubicek and Wang*, 2012] or by using automated ground-based disdrometers originally designed for sizing falling raindrops [*Kruger and Krajewski*, 2002; *Barthazy et al.*, 2004; *Yuter et al.*, 2006]. The results in either case are broadly consistent with LH74, yet the theoretical results assume the surrounding air is still rather than turbulent as would be normal in precipitating storms. Further, video disdrometers that obtain 200 μm resolution silhouettes are subject to quantization and sizing errors [*Yuter et al.*, 2006; *Battaglia et al.*, 2010] and provide insufficient detail to quantify the extent of riming [*Barthazy and Schefold*, 2006; *Brandes et al.*, 2008; *Newman et al.*, 2009]. In the absence of more comprehensive measurements, model fall speed parameterizations are often tuned so that modeled precipitation intensities and distributions in storms match observations [*Colle et al.*, 2005; *Lang et al.*, 2011].

This article presents an initial assessment of how riming and local meteorology affect frozen hydrometeor form, size, and fallspeed distributions using a combination of new measurements obtained at a high-altitude mountain field station in Utah. The centerpiece of the study is the newly developed Multi-Angle Snowflake Camera (MASC) [*Garrett et al.*, 2012]. The MASC automatically photographs hydrometeors in free fall from multiple angles and at high resolution while simultaneously measuring their fallspeed.

2. Measurements

Between January and April 2013, a suite of meteorological and microphysical instruments were deployed to the base of Alta Ski Area, located in Little Cottonwood Canyon in the Wasatch Mountain Range, Utah. Alta Base is at the bottom of Collins Gulch, a side canyon that rises from 2590 m above sea level to the Mount Baldy summit at 3350 m.

At Alta Base, a MASC automatically photographed hydrometeors in free fall using three concentric cameras separated by 36°, each with a focal distance of 10 cm. As described in *Garrett et al.* [2012], two sets of near-infrared emitters and detectors, vertically separated by 32 mm, are used to calculate fallspeed and trigger photographs of hydrometeors larger than about 0.1 mm. The fallspeed is calculated from the time interval between two successive triggers, from top to bottom, provided that they are within 1 s; i.e., the slowest measured fallspeed is 0.03 m s^{-1}. For this study, the camera exposure time was 1/25,000th of a second for the outer two 1.2 MP cameras with 16 mm and 12 mm lenses, and 1/40,000th of a second for the center 5 MP camera with a 25 mm lens. The image resolutions were 26 μm, 14 μm, and 34 μm with respective horizontal fields of view of 33 mm, 33 mm, and 44 mm. Triplet images of hydrometeors and associated fallspeeds were collected at a maximum rate of 2 Hz. Sizing errors associated with the placement of the hydrometeor within the depth of field are anticipated to be approximately 10%, although this error is constrained by multiple camera views.

Past measurements of hydrometeor fallspeeds have normally used a wind skirt or a funnel to still the air first. Recently, it has been found that this approach can lead to sampling biases depending on wind speed and hydrometeor habit and size [*Thériault et al.*, 2012a]. In this study, the MASC was intentionally exposed so that it measured the hydrometeor fallspeed v instead of the terminal velocity v_T.

The MASC was colocated with a vertically pointing METEK 24.1 GHz Micro Rain Radar [*Löffler-Mang et al.*, 1999; *Peters et al.*, 2002]. The Micro Rain Radar (MRR) data are postprocessed to improve data quality and sensitivity using the method of *Maahn and Kollias* [2012]. The minimum detectable echo is approximately −5 dBZ. The MRR obtains a vertical profile every 30 s up to 4.8 km above ground level (agl) with thirty-two 150 m deep range gates. Measurements of snowfall, windspeed, temperature, and relative humidity were obtained throughout Collins Gulch. Here the focus is on temperatures at Mount Baldy summit T_{Baldy} and Alta Base T_{Base}. The respective means and standard deviations during snow events were -10.0 ± 4.9°C and -3.6 ± 4.3°C.

2.1. Effect of Riming on Size Distributions and Fallspeed

A subset of 35,687 hydrometeors was obtained during winter 2013 that satisfied stringent image selection criteria that eliminated focus or coincidence errors that might lead to erroneous fallspeed associations. Prior studies have identified particle form from the ratio of a silhouette's perimeter P to its cross section [*Lindqvist et al.*, 2012; *Schmitt and Heymsfield*, 2014]. An advantage of MASC photographs is that particles are photographed from three angles. Additional shape information can be derived from the mean interpixel brightness variability $\langle\sigma\rangle$ within each image cross section [*Nurzynska et al.*, 2012]. The particle complexity χ is defined as

$$\chi = \frac{P}{2\pi r_{\text{eq}}} (1 + \langle\sigma\rangle) \tag{1}$$

where r_{eq} is the area equivalent radius of the photographed particle cross section and χ is averaged over triplet views. A value of $\chi = 1$ translates to a perfect, homogenous circle.

The complexity metric offers an objective measure for batch processing of hydrometeor type. Riming tends to "round" and "smooth" hydrometeors leading to relatively low values of χ. Classification boundaries are always somewhat subjective. A randomly chosen selection of images shown in Figure 1 illustrates how values of χ less than 1.35 consistently correspond with lump and conical graupel. More aggregated forms have values greater than 1.75. Heavily rimed crystals and aggregates tend to lie in between.

If riming extent is categorized according to complexity χ (Table 1), then, on average, our observations show that increased riming corresponds with more compact and faster falling particles that form under higher temperatures with higher values of column-integrated Doppler spectral width and Doppler velocity. Meteorological contrasts are surprisingly small, however, given the sharper contrasts between graupel and

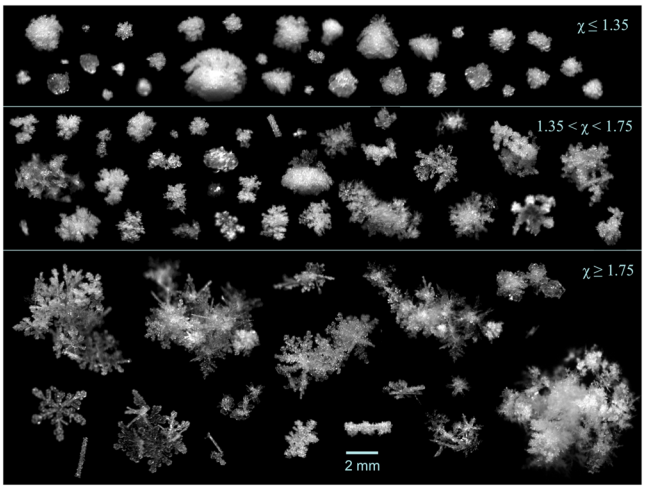

Figure 1. Images obtained from the center camera of the MASC during Wasatch Hydrometeor Aggregation and Riming Experiment categorized according to complexity χ (equation (1)). The pixel resolution is 14 μm.

aggregate form. For example, the average Mount Baldy temperature associated with aggregates is −10.6°C, compared with −8.4°C for graupel; the respective average radar echo depths are 1.40 km and 1.23 km.

Figure 2 shows that riming corresponds with more compact particles that have higher mode and maximum fallspeeds. Normalized size distributions of the particles generally take the form of a gamma function. Looking at the slope of the tail of the distribution λ (e.g., $N\left(D_{\max}\right) = N_0 \exp\left(-\lambda D_{\max}\right)$), values range from 0.69 mm^{-1} for aggregates to 1.99 mm^{-1} for graupel. The slope values are generally consistent with prior observations, although the value for aggregates is lower than the minimum value of 0.9 mm^{-1} that has sometimes been considered possible for generic "snow" [*Braham*, 1990]. On the other hand, it has been suggested that these size distribution measurements may have been steepened by artifacts produced during airborne sampling [*Heymsfield et al.*, 2008].

The relationship between fallspeed and degree of riming in Figure 2 is qualitatively consistent with the results of LH74 who found that aggregates generally fall more slowly than graupel (Table 1). Here the average fallspeed of graupel is 0.90 m s^{-1} compared to 0.72 m s^{-1} for aggregates. What is unusual is that slightly more than one half of each fallspeed distribution had values lower than 0.5 m s^{-1}. In contrast, LH74 observed no graupel that fell slower than 0.8 m s^{-1} and no aggregates that fell slower than 0.5 m s^{-1}.

2.2. The Effect of Size, Turbulence, and Temperature on Fallspeed

What controls the measured fallspeed distributions? The terminal velocity v_T in still air of a given density is determined by particle density, shape, and size [*Böhm*, 1989]. However, because air is turbulent and snowflakes are efficient tracers of atmospheric eddies [*Toloui et al.*, 2014], the terminal velocity may differ from the actual fallspeed v.

To examine this issue more closely, the focus here is on graupel. Graupel is comparatively spherical relative to more complex particle types. Its physical boundaries can be more easily constrained using MASC multiangle images. To determine the relationships between density, size, turbulence, and fallspeed, fluid dynamical calculations are made considering particle size, shape, and orientation using expressions from *Böhm* [1989]. The terminal velocity in still air can be related to a modified Davies number that is a function of the local air density, the circumscribing area projected normal to the vertical $A_{\max}$, the particle cross-section A, and the particle mass. The area equivalent radius is $r_{\mathrm{eq}} = \sqrt{(A/\pi)}$ and a mass estimate is $m = 4\pi\rho r_{\mathrm{eq}}^3/3$.

Using the *Böhm* [1989] expressions, two approaches are taken. The first is to calculate the terminal velocity v_T based on a graupel particle's observed size and shape and an assumed "medium" graupel density ρ_g^{medium}

Table 1. Average Values of Complexity χ, Maximum Dimension $D_{\max}$ (mm), Slope Parameter λ (mm^{-1}), Fallspeed v (m s^{-1}), Temperature at Baldy Summit T_{Baldy} and Alta Base T_{Base} (°C), Radar Echo Depth H (km), and Mean Column Values of Radar Echo Z (dBZ), Doppler Spectral Width SW (m s^{-1}), and Doppler Velocity v_D m s^{-1}[a]

Habit (N)	χ	$D_{\max}$	λ	v	T_{Baldy}	T_{Base}	H	Z	SW	v_D
Aggregates (9,093)	2.00	3.6	0.69	0.72	−10.6	−4.3	1.34	7.2	0.52	0.80
Rimed (18,924)	1.52	2.0	1.19	0.86	−10.3	−3.8	1.35	7.1	0.53	0.83
Graupel (7,670)	1.29	1.4	1.99	0.90	−8.4	−2.1	1.27	7.2	0.62	0.93

[a]Categories are as defined in the text. All quantity means are statistically different at the 95% confidence level using a Kolmogorov-Smirnov test.

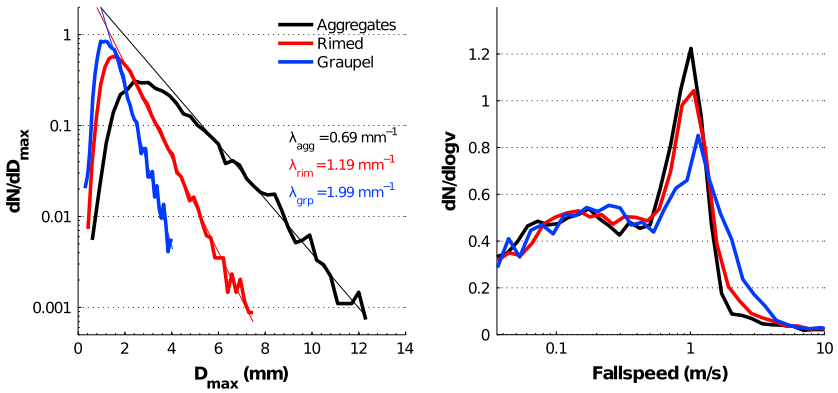

Figure 2. Distributions of (left) maximum dimension D_{max} and (right) fallspeed v obtained by the MASC during 2013, normalized to unity and categorized according to complexity χ (equation (1)). The parameter λ represents the slope of the tail of the distribution.

of 400 kg/m^3 that is commonly used in weather models [e.g., *Rutledge and Hobbs*, 1984; *Meyers et al.*, 1997; *Thompson et al.*, 2004; *Seifert and Beheng*, 2006]. The second is to do the inverse and infer an aerodynamic "effective density" $\rho_g^{aer}(v)$ by assuming that the measured fallspeed v in turbulent air is equivalent to the terminal velocity v_T that is appropriate for still air.

Taking the first approach, the calculated average value of v_T is 2.3 m s^{-1}, which is more than twice as fast as the average graupel fallspeed that was directly measured (Table 1). Taking the second approach, the average value of ρ_g^{aer} is 215 kg m^{-3} or about one half of ρ_g^{medium}. The implication is that ρ_g^{medium} may be an overestimate, at least for high-elevation conditions similar to those at Alta.

LH74 used manual techniques to estimate values for graupel density that lay between 50 kg m^{-3} and 450 kg m^{-3}. While the average values of ρ_g^{aer} from Alta lie within this range, the range of measured fallspeeds shown in Figure 2 is so broad as to imply that a large fraction of graupel particles had very small values of ρ_g^{aer}. In fact, the subset of graupel with fallspeeds below 0.5 m s^{-1} had an average value of ρ_g^{aer} of just 5.6 kg m^{-3}. If this were indeed the physical density ρ_g, it would seem somewhat implausible since it would imply that air made up more than 99% of each particle. Otherwise, graupel particles in the $v < 0.5$ m s^{-1} and $v > 0.5$ m s^{-1} fall speed modes had effectively identical values of the average complexity (1.18) and maximum dimension (1.43 mm). Alta Base temperatures were identical as well (-2°C).

The alternative explanation is that ρ_g^{aer} does not represent the true physical density because the measured fallspeed does not always equal the terminal velocity. To examine the extent to which fallspeed is determined by physical rather than aerodynamic considerations, graupel fallspeed distributions are grouped according to temperature and turbulence, with nominal low and high values defined by the lower and upper quartiles in the total data set.

Temperature measurements from Mount Baldy are used here rather than those from Alta Base since these are the values that are assumed to be closer to the conditions aloft where the graupel formed [*Steenburgh and Alcott*, 2008]. No direct in situ measurement of turbulence was made. Instead, an estimate can be derived from the difference between the maximum wind speed, or gust, that was sampled every 3 s, and the average wind speed from successive 5 min intervals at Alta Base. Following *Schreur and Geertsema* [2008], estimated turbulence is proportional to $E = (\text{Gusts} - \text{Average Wind})^2/2$.

Graupel and meteorological properties separated by temperature and turbulence quartiles are summarized in Table 2. Temperatures higher than −5°C (average −3.5°C) at Mount Baldy were associated with a mean fallspeed of 1.16 m s^{-1} compared with 0.70 m s^{-1} when the temperatures were lower than −13°C (average −17.3°C). The mean aerodynamically derived densities for the high-temperature and low-temperature quartiles were 217 kg m^{-3} and 159 kg m^{-3}, respectively, while the average particle sizes were statistically equivalent. The implication is that graupel that formed at higher temperatures fell faster because it was more dense.

Table 2. As for Table 1, Except med Represents the Median and ρ_g^{aer} Represents the Aerodynamically Derived Graupel Density (kg m^{-3}) Using the Expressions of *Böhm* [1989][a]

Graupel (*N*)	χ	D_{max}	v	v_{med}	ρ_g^{aer}	$\rho_{g\,med}^{aer}$	T_{Baldy}	H	Z	SW	v_D	E
T_{high} (884)	1.18	*1.6*	1.16	0.56	217	44	**−3.5**	1.95	11.3	0.53	0.60	4.0
T_{low} (1079)	1.20	*1.5*	0.70	0.31	159	19	**−17.3**	0.68	3.2	0.61	0.82	2.9
E_{high} (3081)	1.18	*1.5*	0.93	0.33	208	22	−7.9	1.19	7.3	0.75	0.84	**8.1**
E_{low} (555)	1.19	*1.5*	0.96	0.68	162	72	−8.4	1.80	9.0	0.48	0.83	**0.2**

[a]High and low refer to upper and lower quartiles bounded by −5°C and −13°C for Baldy summit temperature T and 3.4 m^2 s^{-2} and 0.4 m^2 s^{-2} for a local measure of turbulence near the MASC E. Quantities whose means are not statistically different at a 95% confidence level are italicized. Mean values of the variables in column 1 are in bold font.

Between the low (0.2 m^2 s^{-2}) and high (8.1 m^2 s^{-2}) turbulence quartiles summarized in Table 2, the average Mount Baldy temperatures and MASC measured fallspeeds were similar. However, with the higher values of E, the median fallspeed shifted from 0.68 to 0.33 m s^{-1}; average values of D_{max} remained unchanged.

Turbulence measured near the MASC tended to extend throughout the column. The column-averaged Doppler spectral width (SW) obtained from the MRR provides a proxy measurement of turbulence further aloft [*Wakasugi et al.*, 1986; *Rinehart*, 2004]. Average values of SW were 60% higher in the upper quartile of E than in the lower quartile. Time-height profiles of MRR SW (not shown) indicate that higher SW values that can occur near the surface can also occur at midlevels in the radar echo.

Figure 3 shows normalized distributions for graupel fallspeed as a function of D_{max}, separated according to the aforementioned temperature and turbulence quartiles. LH74 $v_T\left(D_{max}\right)$ power law relations for lump and conical graupel are superimposed for comparison. The range of values of $v\left(D_{max}\right)$ observed by the MASC are comparatively broad, with an overall bias toward lower values.

Nonetheless, there is a weak similarity between the results presented here and those of LH74, especially when temperatures are high and turbulence is low. For these conditions, there is a similar fallspeed mode near 1 m s^{-1} and also evidence of a linear correlation between log v and log D_{max}. In particular, when turbulence is low, the $v < 0.5$ m s^{-1} mode shown in Figure 2 is much less pronounced. When turbulence is

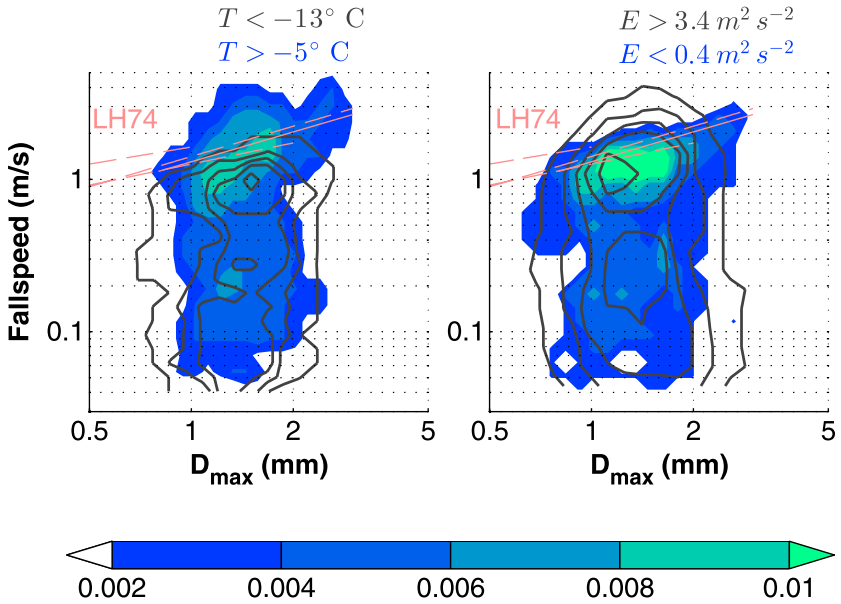

Figure 3. Normalized frequency distributions for graupel as a function of both fallspeed and graupel maximum dimension. Parameterized power law relationships between fallspeed and maximum dimension for conical (solid) and three ranges of lump (dashed) graupel obtained by LH74, and adjusted to 2590 m agl, are shown in red. Black, contoured isolines for high turbulence and low temperatures have equivalent spacing to the colored, filled isolines for low turbulence and high temperatures; the outer contour corresponds to the lowest frequency value of 0.002.

high, however, fallspeeds broaden to both lower and higher values, the $v < 0.5$ m s^{-1} mode becomes more pronounced, and there is no apparent power law relationship between fallspeed and size ($r = -0.05$). At low temperatures, fallspeeds are generally slower, and the power law relationship is also no longer evident ($r = 0.06$).

3. Discussion

Even to the most casual observer it is readily apparent that snow swirls, even in light winds. In fact, *Toloui et al.* [2014] have found that falling snowflakes can be used as fluid tracers to accurately derive turbulent energy spectra for air. The measurements presented here also seem to indicate that the average fallspeed of hydrometeors is determined by turbulence, in addition to particle size and shape.

Studies of the inertial response of particles to turbulence often make a distinction between terminal velocity and the average fallspeed or settling speed W [*Wang and Maxey*, 1993; *Nielsen*, 1993]. With "sweeping," falling particles are accelerated by the downward motions of eddies. "Loitering" buoys faster falling particles in the eddy upward motions. Recent wind tunnel studies by *Good et al.* [2012] point to a continuum in W/v_T with respect to a large-scale settling parameter v_T/v_{rms}, where v_{rms} is the root-mean-squared vertical velocity of the turbulent flow. Sweeping dominates when v_T/v_{rms} is less than about 0.1, in which case W is determined more by v_{rms} than v_T. Otherwise, loitering limits W to as little as one fifth of v_T.

Unfortunately, no measurement of v_{rms} was made adjacent to the MASC that could have been used to directly quantify the level of turbulence. Using nearby wind speeds and gusts as a proxy, the results shown in Figure 3 strongly suggest that turbulence broadens measured fallspeed distributions through both loitering and sweeping. In fact, it erased any sensitivity of fallspeed to particle size that might be attributed to the terminal velocity. This suggests that turbulent eddies played an important if not dominant role in determining the nature of the fallspeed distribution.

As a caveat, it could be that the MASC body disturbed the fallspeed measurements in the presence of high winds, and this is something that will be investigated in the future. Nonetheless, we observed a surprisingly broad range of graupel fallspeeds in even the very stillest air sampled at Alta. Average wind speeds near the MASC in the low E quartile shown in Figure 3 were just 1.2 m s^{-1}. Even so, 25% of graupel had fallspeeds less than 0.17 m s^{-1} and 25% had fallspeeds greater than 1.25 m s^{-1}.

Temperature appears to influence fallspeed more indirectly through its effect on particle density. Wind tunnel studies show that graupel density ρ_g can be related to the impaction speed v_i (m/s) of accreted droplets of radius r (μm) on a surface with temperature T_S (°C) through $\rho_g \propto \left(-rv_i/T_s\right)^{\alpha}$, where α is a constant [*Macklin*, 1962; *Pflaum and Pruppacher*, 1979; *Heymsfield and Pflaum*, 1985; *Rasmussen and Heymsfield*, 1985; *Prodi et al.*, 1986; *Cober and List*, 1993]. *Macklin* [1962] hypothesized that low temperatures and impaction at slow speeds leads to a porous rime. Faster impaction at higher temperature allows liquid to fill any gaps in the rimed structure before freezing to form higher density accretions.

At Alta, we found that a change in T_{Baldy} from −3.5°C to −17.3°C was associated with a 37% reduction in the mean value of the effective density ρ_g^{aer} (Table 2). *Milbrandt and Morrison* [2013] have shown numerically that this relationship between temperature and graupel density introduces an important positive feedback: as graupel falls through higher temperatures, it becomes denser and falls ever faster. This permits solid precipitation that forms within the strong updrafts of a squall line to reach to the surface without requiring a separate model category for hail.

4. Summary

Data from a new instrument that takes high-speed multiangle photographs of hydrometeors in free fall confirm previous work that graupel is more compact and falls faster than aggregates or more lightly rimed particles. A large sample size of simultaneous particle size and fall speed measurements, placed in the context of observations of temperature and turbulence, suggests several refinements to our understanding of the physical characteristics of graupel. An effective density was calculated for graupel based on aerodynamic considerations that is about half the value of 400 kg m^{-3} that is commonly assumed in weather models. Further, the data suggest that graupel formed at lower temperatures is less dense. Strong turbulence broadens the distribution of fallspeeds to the point that the signature relationship of terminal velocity to particle size is no longer evident.

Acknowledgments
This work was supported by the National Science Foundation, award ATM- 1127692. Cale Fallgatter, Konstantin Shkurko, Daniel Howlett, Spencer Rhodes, the Center for Snow Science at Alta, and Alta Ski Area contributed to the instrument development, field operations, and data analysis.The data sets used for this study are archived at http://content.lib.utah.edu/cdm/ref/collection/uspace/id/10605.

The Editor thanks Darrel Gibson Baumgardner and an anonymous reviewer for their assistance in evaluating this paper.

References

Barthazy, E., and R. Schefold (2006), Fall velocity of snowflakes of different riming degree and crystal types, *Atmos. Res.*, *82*, 391–398.
Barthazy, E., S. Göke, R. Schefold, and D. Högl (2004), An optical array instrument for shape and fall velocity measurements of hydrometeors, *J. Atmos. Oceanic Technol.*, *21*, 1400–1416, doi:10.1175/1520-0426(2004)021.
Battaglia, A., E. Rustemeier, A. Tokay, U. Blahak, and C. Simmer (2010), Parsivel snow observations: A critical assessment, *J. Atmos. Oceanic Technol.*, *27*(2), 333–344, doi:10.1175/2009JTECHA1332.1.
Böhm, H. P. (1989), A general equation for the terminal fall speed of solid hydrometeors, *J. Atmos. Sci.*, *46*, 2419–2427, doi:10.1175/1520-0469(1989)046<2419:AGEFTT>2.0.CO;2.
Braham, R. R. (1990), Snow particle size spectra in lake effect snows, *J. Appl. Meteor.*, *29*(3), 200–207, doi:10.1175/1520-0450(1990)029<0200:SPSSIL>2.0.CO;2.
Brandes, E. A., K. Ikeda, G. Thompson, and M. Schönhuber (2008), Aggregate terminal velocity/temperature relations, *J. Appl. Meteorol. Clim.*, *47*, 2729–2736, doi:10.1175/2008JAMC1869.1.
Cober, S. G., and R. List (1993), Measurements of the heat and mass transfer parameters characterizing conical graupel growth, *J. Atmos. Sci.*, *50*(11), 1591–1609, doi:10.1175/1520-0469(1993)050<1591:MOTHAM>2.0.CO;2.
Colle, B. A., M. F. Garvert, J. B. Wolfe, C. F. Mass, and C. P. Woods (2005), The 13–14 December 2001 IMPROVE-2 Event. Part III: Simulated microphysical budgets and sensitivity studies, *J. Atmos. Sci.*, *62*, 3535–3558, doi:10.1175/JAS3552.1.
Garrett, T. J., C. Fallgatter, K. Shkurko, and D. Howlett (2012), Fall speed measurement and high-resolution multi-angle photography of hydrometeors in free fall, *Atmos. Meas. Tech.*, *5*(11), 2625–2633, doi:10.5194/amt-5-2625-2012.
Garvert, M. F., C. P. Woods, B. A. Colle, C. F. Mass, P. V. Hobbs, M. T. Stoelinga, and J. B. Wolfe (2005), The 13–14 December 2001 IMPROVE-2 Event. Part II: Comparisons of MM5 model simulations of clouds and precipitation with observations, *J. Atmos. Sci.*, *62*, 3520–3534, doi:10.1175/JAS3551.1.
Good, G. H., S. Gerashchenko, and Z. Warhaft (2012), Intermittency and inertial particle entrainment at a turbulent interface: The effect of the large-scale eddies, *J. Fluid Mech.*, *694*, 371–398, doi:10.1017/jfm.2011.552.
Heymsfield, A. J., and J. C. Pflaum (1985), A quantitative assessment of the accuracy of techniques for calculating graupel growth, *J. Atmos. Sci.*, *42*(21), 2264–2274, doi:10.1175/1520-0469(1985)042<2264:AQAOTA>2.0.CO;2.
Heymsfield, A. J., and C. D. Westbrook (2010), Advances in the estimation of ice particle fall speeds using laboratory and field measurements, *J. Atmos. Sci.*, *67*, 2469–2482, doi:10.1175/2010JAS3379.1.
Heymsfield, A. J., P. Field, and A. Bansemer (2008), Exponential size distributions for snows, *J. Atmos. Sci.*, *65*(12), 4017–4031, doi:10.1175/2008JAS2583.1.
Hong, S., J. Dudhia, and S. Chen (2004), A revised approach to ice microphysical processes for the bulk parameterization of clouds and precipitation, *Mon. Weather Rev.*, *132*, 103–120, doi:10.1175/1520-0493(2004)132<0103:ARATIM>2.0.CO;2.
Iguchi, T., T. Matsui, J. J. Shi, W.-K. Tao, A. P. Khain, A. Hou, R. Cifelli, A. Heymsfield, and A. Tokay (2012), Numerical analysis using WRF-SBM for the cloud microphysical structures in the C3VP field campaign: Impacts of supercooled droplets and resultant riming on snow microphysics, *J. Geophys. Res.*, *117*, D23206, doi:10.1029/2012JD018101.
Khvorostyanov, V. I., and J. A. Curry (2002), Terminal velocities of droplets and crystals: Power laws with continuous parameters over the size spectrum, *J. Atmos. Sci.*, *59*, 1872–1884, doi:10.1175/1520-0469(2002)059<1872:TVODAC>2.0.CO;2.
Kruger, A., and W. F. Krajewski (2002), Two-dimensional video disdrometer: A description, *J. Atmos. Oceanic Technol.*, *19*, 602–617.
Kubicek, A., and P. K. Wang (2012), A numerical study of the flow fields around a typical conical graupel falling at various inclination angles, *Atmos. Res.*, *118*, 15–26, doi:10.1016/j.atmosres.2012.06.001.
Lang, S. E., W.-K. Tao, X. Zeng, and Y. Li (2011), Reducing the biases in simulated radar reflectivities from a bulk microphysics scheme: Tropical convective systems, *J. Atmos. Sci.*, *68*(10), 2306–2320.
Lin, Y., and B. A. Colle (2011), A new bulk microphysical scheme that includes riming intensity and temperature dependent ice characteristics, *Mon. Weather Rev.*, *139*, 1013–1035, doi:10.1175/2010MWR3293.1.
Lin, Y., L. J. Donner, and B. A. Colle (2010), Parameterization of riming intensity and its impact on ice fall speed using arm data, *Mon. Weather Rev.*, *139*(3), 1036–1047, doi:10.1175/2010MWR3299.1.
Lin, Y. L., R. D. Farley, and H. D. Orville (1983), Bulk parameterization of the snow field in a cloud model, *J. Clim. Appl. Meteorol.*, *22*, 1065–1092.
Lindqvist, H., K. Muinonen, T. Nousiainen, J. Um, G. M. McFarquhar, P. Haapanala, R. Makkonen, and H. Hakkarainen (2012), Ice-cloud particle habit classification using principal components, *J. Geophys. Res.*, *117*, D16206, doi:10.1029/2012JD017573.
Liu, C., K. Ikeda, G. Thompson, R. Rasmussen, and J. Dudhia (2011), High-resolution simulations of wintertime precipitation in the Colorado headwaters region: Sensitivity to physics parameterizations, *Mon. Weather Rev.*, *139*(11), 3533–3553.
Locatelli, J. D., and P. V. Hobbs (1974), Fall speeds and masses of solid precipitation particles, *J. Geophys. Res.*, *79*, 2185–2197, doi:10.1029/JC079i015p02185.
Löffler-Mang, M., M. Kunz, and W. Schmid (1999), On the performance of a low-cost K-band Doppler radar for quantitative rain measurements, *J. Atmos. Oceanic Tech.*, *16*, 379–387, doi:10.1175/1520-0426(1999)016<0379:OTPOAL>2.0.CO;2.
Maahn, M., and P. Kollias (2012), Improved Micro Rain Radar snow measurements using Doppler spectra post-processing, *Atmos. Meas. Tech.*, *5*(11), 2661–2673.
Macklin, W. C. (1962), The density and structure of ice formed by accretion, *Q. J. R. Meteorol. Soc.*, *88*(375), 30–50, doi:10.1002/qj.49708837504.
Meyers, M. P., R. L. Walko, J. Y. Harrington, and W. R. Cotton (1997), New {RAMS} cloud microphysics parameterization. Part II: The two-moment scheme, *Atmos. Res.*, *45*(1), 3–39, doi:10.1016/S0169-8095(97)00018-5.
Milbrandt, J. A., and H. Morrison (2013), Prediction of graupel density in a bulk microphysics scheme., *J. Atmos. Sci.*, *70*(2), 410–429.
Milbrandt, J. A., M. K. Yau, J. Mailhot, S. Bélair, and R. McTaggart-Cowan (2010), Simulation of an orographic precipitation event during IMPROVE-2. Part II: Sensitivity to the number of moments in the bulk microphysics scheme, *Mon. Weather Rev.*, *138*, 625–642, doi:10.1175/2009MWR3121.1.
Mitchell, D. L. (1996), Use of mass- and area-dimensional power laws for determining precipitation particle terminal velocities, *J. Atmos. Sci.*, *53*, 1710–1723, doi:10.1175/1520-0469(1996)053.
Newman, A. J., P. A. Kucera, and L. F. Bliven (2009), Presenting the Snowflake Video Imager (SVI), *J. Atmos. Oceanic. Technol.*, *26*, 167–179, doi:10.1175/2008JTECHA1148.1.
Nielsen, P. (1993), Turbulence effects on the settling of suspended particles, *J. Sediment. Petrol.*, *63*, 835–838.
Nurzynska, K., M. Kubo, and K. ichiro Muramoto (2012), Texture operator for snow particle classification into snowflake and graupel, *Atmos. Res.*, *118*, 121–132, doi:10.1016/j.atmosres.2012.06.013.

Peters, G., B. Fischer, and T. Andersson (2002), Rain observations with a vertically looking Micro Rain Radar (MRR), *Boreal Environ. Res.*, *7*, 353–362.

Pflaum, J. C., and H. R. Pruppacher (1979), A wind tunnel investigation of the growth of graupel initiated from frozen drops, *J. Atmos. Sci.*, *36*(4), 680–689, doi:10.1175/1520-0469(1979)036<0680:AWTIOT>2.0.CO;2.

Prodi, F., L. Levi, and P. Pederzoli (1986), The density of accreted ice, *Q. J. R. Meteorol. Soc.*, *112*(474), 1081–1090, doi:10.1002/qj.49711247409.

Rasmussen, R. M., and A. J. Heymsfield (1985), A generalized form for impact velocities used to determine graupel accretional densities, *J. Atmos. Sci.*, *42*(21), 2275–2279, doi:10.1175/1520-0469(1985)042<2275:AGFFIV>2.0.CO;2.

Reisner, J., R. M. Rasmussen, and R. T. Bruintjes (1998), Explicit forecasting of supercooled liquid water in winter storms using the MM5 mesoscale model, *Q. J. R. Meteorol. Soc.*, *124*, 1071–1107, doi:10.1256/smsqj.54803.

Rinehart, R. (2004), A solution of the problem of rapid scanning for radar antennae, *J. Appl. Phys.*, *19*(9), 860–862.

Rutledge, S. A., and P. V. Hobbs (1984), The mesoscale and microscale structure and organization of clouds and precipitation in mid-latitude cyclones. XII: A diagnostic modeling study of precipitation development in narrow cold-frontal rainbands, *J. Atmos. Sci.*, *41*, 2949–2972, doi:10.1175/1520-0469(1984)041<2949:TMAMSA>2.0.CO;2.

Schmitt, C. G., and A. J. Heymsfield (2014), Observational quantification of the separation of simple and complex atmospheric ice particles, *Geophys. Res. Lett.*, *41*, 1301–1307, doi:10.1002/2013GL058781.

Schreur, B. W., and G. Geertsema (2008), Theory for a TKE based parameterization of wind gusts, *HIRLAM Newslett.*, *54*, 177–188.

Seifert, A., and K. D. Beheng (2006), A two-moment cloud microphysics parameterization for mixed-phase clouds. Part 2: Maritime vs. continental deep convective storms, *Meteorol. Atmos. Phys.*, *92*(1-2), 67–82, doi:10.1007/s00703-005-0113-3.

Steenburgh, W. J., and T. I. Alcott (2008), Secrets of the "Greatest Snow on Earth", *Bull. Am. Meteorol. Soc.*, *89*, 1285–1293.

Tao, W.-K., et al. (2003), Microphysics, radiation and surface processes in the Goddard Cumulus Ensemble (GCE) model, *Meteorol. Atmos. Phys.*, *82*(1), 97–137.

Thériault, J. M., R. Rasmussen, K. Ikeda, and S. Landolt (2012a), Dependence of snow gauge collection efficiency on snowflake characteristics, *J. Appl. Meteorol. Climatol.*, *51*, 745–762, doi:10.1175/JAMC-D-11-0116.1.

Thériault, J. M., R. E. Stewart, and W. Henson (2012b), Impacts of terminal velocity on the trajectory of winter precipitation types, *Atmos. Res.*, *116*, 116–129, doi:10.1016/j.atmosres.2012.03.008.

Thompson, G., R. M. Rasmussen, and K. Manning (2004), Explicit forecasts of winter precipitation using an improved bulk microphysics scheme. Part I: Description and sensitivity analysis, *Mon. Weather Rev.*, *132*(2), 519–542, doi:10.1175/1520-0493(2004)132<0519:EFOWPU>2.0.CO;2.

Toloui, M., S. Riley, J. Hong, K. Howard, L. Chamorro, M. Guala, and J. Tucker (2014), Measurement of atmospheric boundary layer based on super-large-scale particle image velocimetry using natural snowfall, *Exper. Fluids*, *55*(5), 1–14, doi:10.1007/s00348-014-1737-1.

Wakasugi, K., A. Mizutani, M. Matsuo, S. Fukao, and S. Kato (1986), A direct method for deriving drop-size distribution and vertical air velocities from VHF Doppler radar spectra, *J. Atmos. Oceanic Technol.*, *3*(4), 623–629.

Wang, L.-P., and M. R. Maxey (1993), Settling velocity and concentration distribution of heavy particles in homogeneous isotropic turbulence, *J. Fluid Mech.*, *256*, 27–68, doi:10.1017/S0022112093002708.

Yuter, S. E., D. E. Kingsmill, L. B. Nance, and M. Löffler-Mang (2006), Observations of precipitation size and fall speed characteristics within coexisting rain and wet snow, *J. Appl. Meteorol. Clim.*, *45*, 1450–1464, doi:10.1175/JAM2406.1.